SAE International

Effect of Flow on Helmholtz Resonator Acoustics: A Three-Dimensional Computational Study vs. Experiments

2011-01-1521
Published
05/17/2011

Emel Selamet
Ohio State Univ.

Ahmet Selamet
Ohio State Univ

Asim Iqbal and Hyunsu Kim
Ohio State Univ.

doi:10.4271/2011-01-1521

ABSTRACT

The effectiveness of the Helmholtz resonator as a narrow band acoustic attenuator, particularly at low frequencies, makes it a highly desirable component in a wide variety of applications, including engine breathing systems. The present study investigates the influence of mean flow grazing over the neck of such a configuration on its acoustic performance both computationally and experimentally. Three-dimensional unsteady, turbulent, and compressible Navier-Stokes equations are solved by using the Pressure-Implicit-Splitting-of-Operators algorithm in STAR-CD to determine the time-dependent flow field. The introduction of mean flow in the main duct is shown to reduce the peak transmission loss and shift the fundamental resonance frequency to a higher value. The predictions for transmission loss exhibit a good agreement with the experimental results obtained on a flow-impedance tube, thereby demonstrating the effectiveness of the computational approach in studying the complex interactions of the flow field with the acoustics of Helmholtz resonators.

1. INTRODUCTION

Extensive use of Helmholtz resonators in noise control has led to numerous studies concentrating primarily on the effect of geometry on their acoustic performance, and in the absence of flow. A discussion of pertinent literature both on the impact of geometrical variations as well as the computational methodology to predict the acoustic response has been provided recently [1,2]. These effective narrow band attenuators are, however, frequently implemented in ducts with mean flow, including engine breathing systems. Therefore, a better understanding of the flow effect on acoustics and particularly the ability to predict the complex fluid physics near the resonator-duct interface are critical to the design of these configurations.

Earlier investigations of the flow effect on the acoustic behavior of Helmholtz resonators are experimental, starting presumably by McAuliffe [3]. Meyer *et al.* [4] investigated the effect of flow velocity on the attenuation of an array of Helmholtz resonators. Philips [5] observed that the acoustic resistance of the neck increases linearly with flow velocity. This increase in resistance was also shown to coincide with the decrease in the estimated end correction. Philips used these observations to explain the linear increase in the fundamental resonance frequency with velocity. Anderson [6] also noted a linear increase in the fundamental resonance frequency with mean flow past a single sidebranch Helmholtz resonator. Through experiments and semi-empirical predictions, Hersh *et al.* [7] demonstrated that the Helmholtz resonator exhibits a linear increase in acoustic resistance and a diminishing reactance with grazing flow.

While these experimental findings are clearly helpful in quantifying the effect of flow on the acoustics of Helmholtz resonators, the design of an effective configuration requires the availability of analytical and/or computational techniques capable of accurately capturing the fluid physics. The complexity of the unsteady, nonlinear, viscous, and compressible flows renders the analytical methods insufficient in modeling the inherent physics, leading ultimately to the employment of computational techniques. Cummings [8] presented one of the earliest numerical investigations on the effect of grazing fully developed flow on the acoustics of a Helmholtz resonator. He demonstrated that a quasi one-dimensional (1D) time domain numerical approach accounting for the flow effect on acoustic resistance of the resonator could predict the cavity pressure with reasonable accuracy. More recently, Ricot *et al.* [9] investigated "sunroof buffeting" (unsteady flow past a Helmholtz-like cavity) computationally using a Lattice Boltzmann Method solver; and Tam and Kurbatskii [10] and Tam *et al.* [11] used direct numerical simulation (DNS) to investigate the dissipation mechanism for acoustic liners comprised of Helmholtz resonators. As the acoustic performance of noise suppression devices is typically judged by their transmission loss (TL) characteristics, TL will be carefully assessed here on the evaluation of flow effect on the Helmholtz resonator acoustics. While experimental investigations of the flow effect on the transmission loss of these resonators are limited, there is no three-dimensional (3D) computational study on this specific aspect to the authors' knowledge. Recently, Iqbal and Selamet [12] used a non-commercial two-dimensional (2D) Navier-Stokes solver, implementing the Pressure-Implicit-Splitting-of-Operators (PISO) algorithm, to examine the effect of flow velocities over the range 0-100 m/s on the transmission loss of a Helmholtz resonator. While this investigation successfully captured some of the trends observed in prior experimental studies [3, 4, 5, 6, 7], due to its 2D nature of the geometry combined at the time with the absence of an experimental facility capable of accommodating flow, it lacked comparisons with experiments performed on realistic configurations. The objective of the present study is therefore to improve upon the constraints of this earlier work [12] by introducing (1) a 3D CFD approach in time-domain to examine the effect of mean flow on the transmission loss of a Helmholtz resonator and (2) performing experiments with the same resonator configuration on a new flow-impedance tube setup and providing a comparison.

Following this Introduction, Section 2 briefly describes the computational approach and Section 3 the experimental technique used in this study. Computational results as well as their comparison with experimental data are presented in Section 4, followed by concluding remarks in Section 5.

2. THREE-DIMENSIONAL COMPUTATIONAL APPROACH

For accurate prediction of transmission loss, it is imperative that the numerical method captures the flow field properly, particularly at the neck-main duct interface. Solving the unsteady viscous compressible flow equations accurately allows for the effects of acoustic wave propagation and bulk fluid flow to be determined simultaneously. Due to the three-dimensional nature of the current study, the conservation equations [13] to be solved by STAR-CD for a compressible Newtonian fluid are presented here in their 3D form (after neglecting the source terms) as

Conservation of Mass:

$$\frac{\partial \rho}{\partial t} + \frac{\partial}{\partial x_j}\left(\rho u_j\right) = 0\,; \tag{1}$$

Conservation of Momentum:

$$\frac{\partial}{\partial t}(\rho u_i) + \frac{\partial}{\partial x_j}\left(\rho u_j u_i\right) = -\frac{\partial p}{\partial x_i} + \frac{\partial}{\partial x_j}\left[\mu\left(\frac{\partial u_i}{\partial x_j} + \frac{\partial u_j}{\partial x_i}\right) - \frac{2}{3}\mu\frac{\partial u_k}{\partial x_k}\delta_{ij} - \overline{\rho u_i' u_j'}\right]; \tag{2}$$

Conservation of Energy:

$$\frac{\partial}{\partial t}(\rho h_t) + \frac{\partial}{\partial x_j}\left(\rho h_t u_j\right) = \frac{\partial p}{\partial t} + u_j\frac{\partial p}{\partial x_j} + \left(\mu\left(\frac{\partial u_i}{\partial x_j} + \frac{\partial u_j}{\partial x_i}\right) - \frac{2}{3}\mu\frac{\partial u_k}{\partial x_k}\delta_{ij} - \overline{\rho u_i' u_j'}\right)\frac{\partial u_i}{\partial x_j} + \frac{\partial}{\partial x_j}\left(\kappa\frac{\partial T}{\partial x_j} - \overline{\rho u_j' h_t'}\right) \tag{3}$$

where $h_t = \bar{c}_p T - c_p^o T_o$ is the thermal enthalpy;

Equation of State:

$$p = \rho R T\,. \tag{4}$$

Repeated subscripts denote summation, for example, $\frac{\partial \rho u_j}{\partial x_j} = \frac{\partial \rho u_1}{\partial x_1} + \frac{\partial \rho u_2}{\partial x_2} + \frac{\partial \rho u_3}{\partial x_3} = \frac{\partial \rho u}{\partial x} + \frac{\partial \rho v}{\partial y} + \frac{\partial \rho w}{\partial z}$. In Eqs. (1), (2), (3), (4), the different spatial components of velocity, pressure, and other dependent variables, including viscous stresses, assume their ensemble average values, where u_i' are

fluctuations about the ensemble average velocity with the overbar representing the ensemble averaging process.

The terms involving the fluctuating velocities correspond to Reynolds stresses due to turbulent motion and are linked to the mean velocity field via the turbulence models. For turbulence modeling STAR-CD offers several options, including Eddy Viscosity, Reynolds Stress, Large Eddy Simulation (LES), and Detached Eddy Simulation (DES) models. The present work has chosen the low Reynolds number k - ε turbulence model [14,15] for turbulence calculations. The differential equations associated with the k - ε turbulence model (after neglecting the effects of buoyancy forces) are expressed [13] as:

Turbulent Kinetic Energy (k):

$$\frac{\partial}{\partial t}(\rho k)+\frac{\partial}{\partial x_j}(\rho u_j k)=\frac{\partial}{\partial x_j}\left(\left(\mu+\frac{\mu_t}{\sigma_k}\right)\frac{\partial k}{\partial x_j}\right) + \mu_t \mathcal{P}-\rho\varepsilon-\frac{2}{3}\left(\mu_t\frac{\partial u_i}{\partial x_i}+\rho k\right)\frac{\partial u_i}{\partial x_i}+\mu_t\mathcal{P}_{NL} \tag{5}$$

where $\mathcal{P}=\left(\frac{\partial u_i}{\partial x_j}+\frac{\partial u_j}{\partial x_i}\right)\frac{\partial u_i}{\partial x_j}$, $\mathcal{P}_{NL}=-\frac{\rho}{\mu_t}\overline{u_i' u_j'}\frac{\partial u_i}{\partial x_j}-\left[\mathcal{P}-\frac{2}{3}\left(\frac{\partial u_i}{\partial x_i}+\frac{\rho k}{\mu_t}\right)\frac{\partial u_i}{\partial x_i}\right]$, σ_k is the turbulent Prandtl number, and μ_t is the turbulent viscosity;

Turbulent Dissipation (ε):

$$\frac{\partial}{\partial t}(\rho\varepsilon)+\frac{\partial}{\partial x_j}(\rho u_j\varepsilon)=\frac{\partial}{\partial x_j}\left[\left(\mu+\frac{\mu_t}{\sigma_\varepsilon}\right)\frac{\partial\varepsilon}{\partial x_j}\right] + C_{\varepsilon 1}\frac{\varepsilon}{k}\left\{\mu_t\left(\mathcal{P}+\mathcal{P}_{NL}+\mathcal{P}'\right)-\frac{2}{3}\left(\mu_t\frac{\partial u_i}{\partial x_i}+\rho k\right)\frac{\partial u_i}{\partial x_i}\right\} - C_{\varepsilon 2}\left(1-0.3e^{-R_t^2}\right)\rho\frac{\varepsilon^2}{k}+C_{\varepsilon 4}\rho\varepsilon\frac{\partial u_i}{\partial x_i} \tag{6}$$

where σ_ε is the turbulent Prandtl number, $\mathcal{P}'=1.33\left[1-0.3e^{-R_t^2}\right]\left[\mathcal{P}+\mathcal{P}_{NL}+2\frac{\mu}{\mu_t}\frac{k}{y^2}\right]e^{-0.00375Re_y^2}$, $R_t=\frac{k^2}{\nu\varepsilon}$, $Re_y=\frac{y\sqrt{k}}{\nu}$, and y is the normal distance to the nearest wall.

STAR-CD implements multiple solution algorithms out of which the PISO algorithm [16, 17, 18] has been selected for solving Eqs. (1), (2), (3), (4), (5), (6). The PISO algorithm is an implicit, noniterative method for solving unsteady compressible flow equations. Solving the full Navier-Stokes equations facilitates the proper modeling of nonlinearities in acoustic waves as it overcomes the constraints of small wave amplitude treatments. Additionally, it permits the interaction between vortices and acoustic waves, with each affecting the other until a natural equilibrium is reached. Standard values were implemented for the relevant k - ε parameters as illustrated in Table 1.

Table 1. k - ε turbulence model parameters.

C_μ	σ_k	σ_ε	$C_{\varepsilon 1}$	$C_{\varepsilon 2}$	$C_{\varepsilon 4}$	κ
0.09	1	1.219	1.44	1.92	-0.33	0.419

Figure 1 illustrates a schematic of the 3D geometry used in computations. The inlet (between x = 0 and Helmholtz neck) and outlet (between Helmholtz neck and outlet) ducts have a diameter of 4.859 cm and lengths of L_{in}= L_{out}= 48.99 cm. The Helmholtz volume has a diameter of 15.32 cm and is 24.42 cm long while its neck has a diameter and length of 4.044 cm and 8.05 cm, respectively. The computational mesh is depicted in Figure 2. A fine mesh has been selected with a total of 60,031 cells over the computational domain to allow for proper resolution of the shear layer and vortices at the neck-duct interface. Following numerical trials, a time step of 4.1615×10^{-5} s has been chosen and retained in all runs, providing sufficient accuracy. Decreasing the time step further, for example, had no impact on transmission loss at selected frequencies.

For all computations performed in this study, flow enters from the left and leaves from the right (recall Fig. 1). Solid wall boundary conditions with no slip are imposed at all surfaces. At the inlet, a time-varying velocity

$$u(x=0)=u_{in}+a_{in}\sin(\omega t), \tag{7}$$

is imposed for the x component along with v(=0)and w(=0), where u_{in} is the mean flow velocity in [m/s], a_{in} = 0.01 m/s the perturbation amplitude, and $\omega = 2\pi f$ the angular frequency. Also specified at the same location are temperature T, density ρ, turbulent kinetic energy k, and turbulent dissipation ε. Temperature and density at the inlet are then used in ideal gas relationship to determine the pressure. The outlet is modeled as an anechoic termination through a "transient-wave transmissive boundary" condition that allows pressure waves to escape without reflection. The transient-wave transmissive boundary follows an approach similar to that for stationary shocks. For given 'free stream' conditions, wave theory is used to calculate the magnitude and direction of the flow at the transmissive boundary [13]. The entire domain is initially (t = 0) set to u(=0), v(=0),

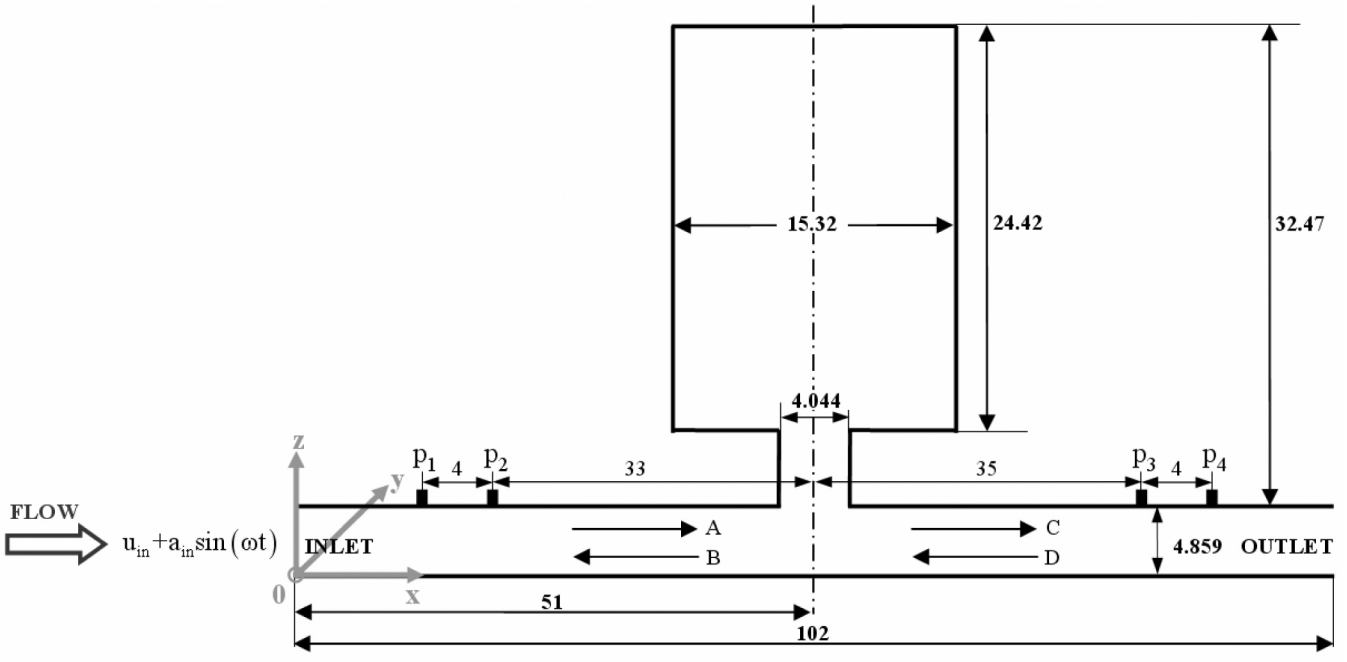

Figure 1. Schematic of the setup used in computations (dimensions in cm).

w(=0), p = 101 kPa, and T = 293 K. Once all the boundary and initial conditions are specified, the solver is allowed to run until the only change in pressure with time, at a fixed point, is the acoustic oscillations, indicating that a quasi-steady state has been reached. The two-microphone technique of Chung and Blaser [19,20] is then applied in the present study under the condition of equal cross-sectional areas at upstream and downstream locations yielding the transmission loss as

$$TL = 20\log_{10}\left|\frac{P_1(f)e^{ik_r s} - P_2(f)}{P_3(f)e^{ik_r s} - P_4(f)}\right|, \qquad (8)$$

where $P_1(f)$, $P_2(f)$, $P_3(f)$, and $P_4(f)$ are the Fourier-transformed acoustic pressures in the frequency domain at the four "microphone" locations shown in Fig. 1, $k_r = k / (1 - M)$ is the wavenumber of the reflected wave component where M is the Mach number, and s (=0.04 m) is the microphone spacing. Once the computations reach a quasi-steady state, pressures computed at locations 1-4 are sampled over a specific time duration. As the STAR-CD solver performs computations in the time domain, the predictions are transformed to the frequency domain by taking fast Fourier transforms (FFTs) of the computed pressures. The transmission loss is then determined by applying Eq. (8) to pressures in the frequency domain.

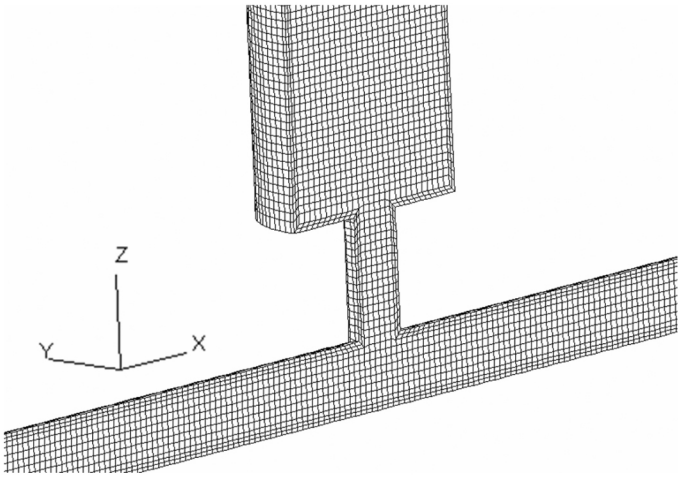

Figure 2. Clipped section of the 3D computational mesh near the neck-duct interface.

3. EXPERIMENTAL SETUP

A new flow-impedance tube setup, shown in Fig. 3, has been used to measure the transmission loss of the Helmholtz resonator in the presence of mean flow. Two loudspeakers are driven by a signal generator module (B&K 3107) linked to a 100 W amplifier. The acoustic fluctuations at both upstream and downstream of the component are measured by a pair of two ¼ in condenser microphones (B&K 4135) which are mounted 4 cm apart flush with inner surface of 4.859 cm diameter main duct. The microphone signals are post-processed by a multi-channel signal analyzer (B&K 3550). Each measurement involves averaging 100 ensembles to

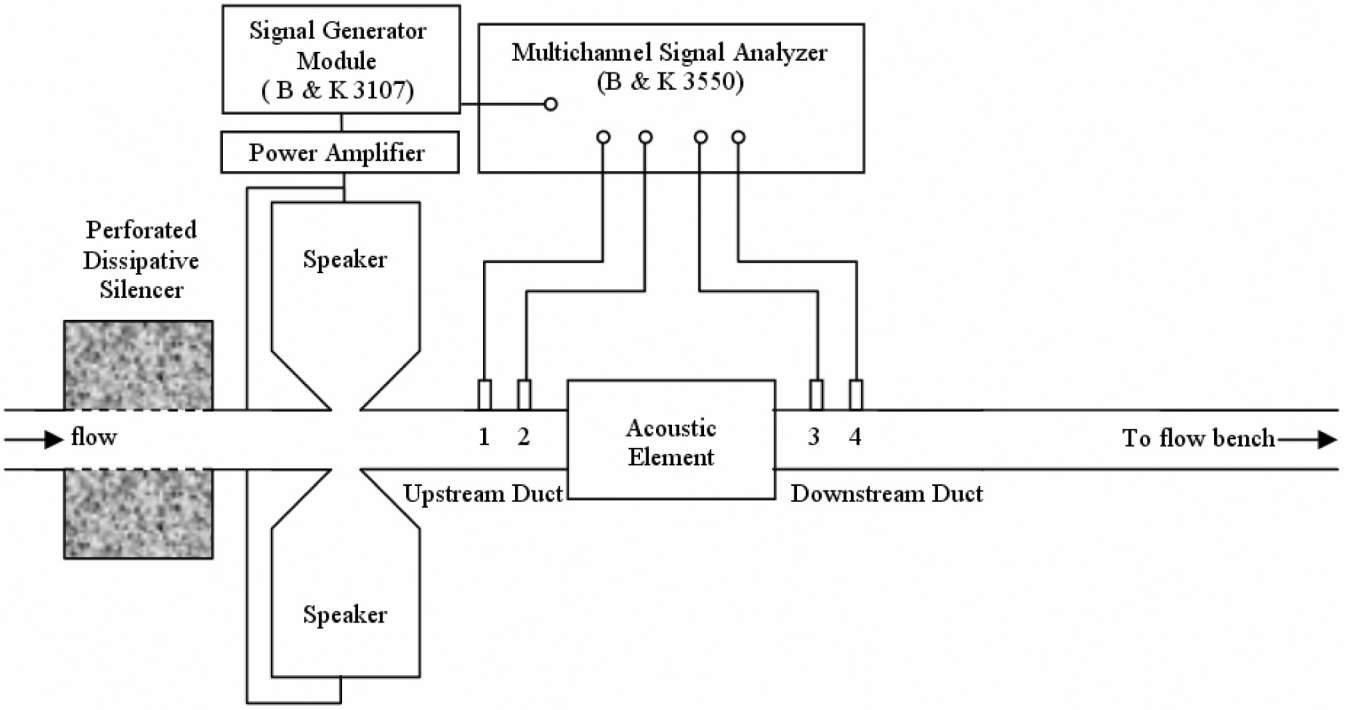

Figure 3. Impedance tube setup in the presence of flow.

reduce the signal noise. Microphone switching method established by Chung and Blaser [19,20] is employed to compensate for the mismatch of magnitude and phase among microphones. The downstream side is connected to a flow bench which is capable of generating a maximum air flow rate of 0.63 kg/s at standard conditions with a pressure drop of up to 8.72 kPa through a conical tube (with the inner diameter increasing gradually from 4.859 cm to 7.62 cm over a length of 3.05 m, hence a very small half angle of 0. 256°) followed by a 33 m long flexible tube of 7.62 cm inner diameter. The conical tube is incorporated to provide a smooth transition with a low reflection coefficient at the frequency range of interest, thereby allowing a larger diameter flexible tube to follow without excessive flow losses. The purpose of the long flexible tube is to enable signal separation in the time domain, as described next. A dissipative silencer is also installed on the upstream side to reduce the flow noise.

The measurement of transmission loss requires the acoustic powers of the incident and transmitted waves. The incident wave on the upstream side is measured in the frequency domain by wave decomposition utilizing two microphones [21]. The measurement of the transmitted wave on the downstream side relies on a signal separation in time domain by introducing a transient input (burst random or burst sine in the present study) traveling through the long tube. While burst random used in the absence of flow facilitates a rapid measurement, it has relatively low power compared to burst sine which concentrates the input power on a single frequency. Burst sine is, therefore, chosen in the presence of flow for improved signal-to-noise ratio and swept for the frequency range of interest with an automated arrangement. Burst signals of 0.2 s duration are generated and fed into the main duct during a total of 1 s measurement time. The combined length (36 m) of the conical transition and flexible tube leads to about 0.21 s delay (based on a speed of sound of 343 m/s at the room temperature) until the wave reflected from the other end of the flexible tube reaches the downstream microphone. The transient time window with the same 0.2 s duration has been, therefore, applied to time series before the reflected wave comes back to the microphone. The foregoing technique ensures reflection coefficients to be lower than 0.1 at the frequency range of interest in the present study. The transmission loss can then be obtained from

$$TL = 10\log_{10}\left|\frac{P_u(f)}{P_d(f)}\right|^2, \tag{9}$$

where P_u (f) represents the incident wave on the upstream side and P_d (f) the transmitted wave on the downstream side, both in the frequency domain.

4. RESULTS AND DISCUSSION

By applying the 3D computational approach described earlier in Section 2 to the Helmholtz resonator of Fig. 1 (and 2), the transmission loss is predicted at discrete frequencies as shown in Fig. 4 for no-flow (M = 0) as well as two flow cases

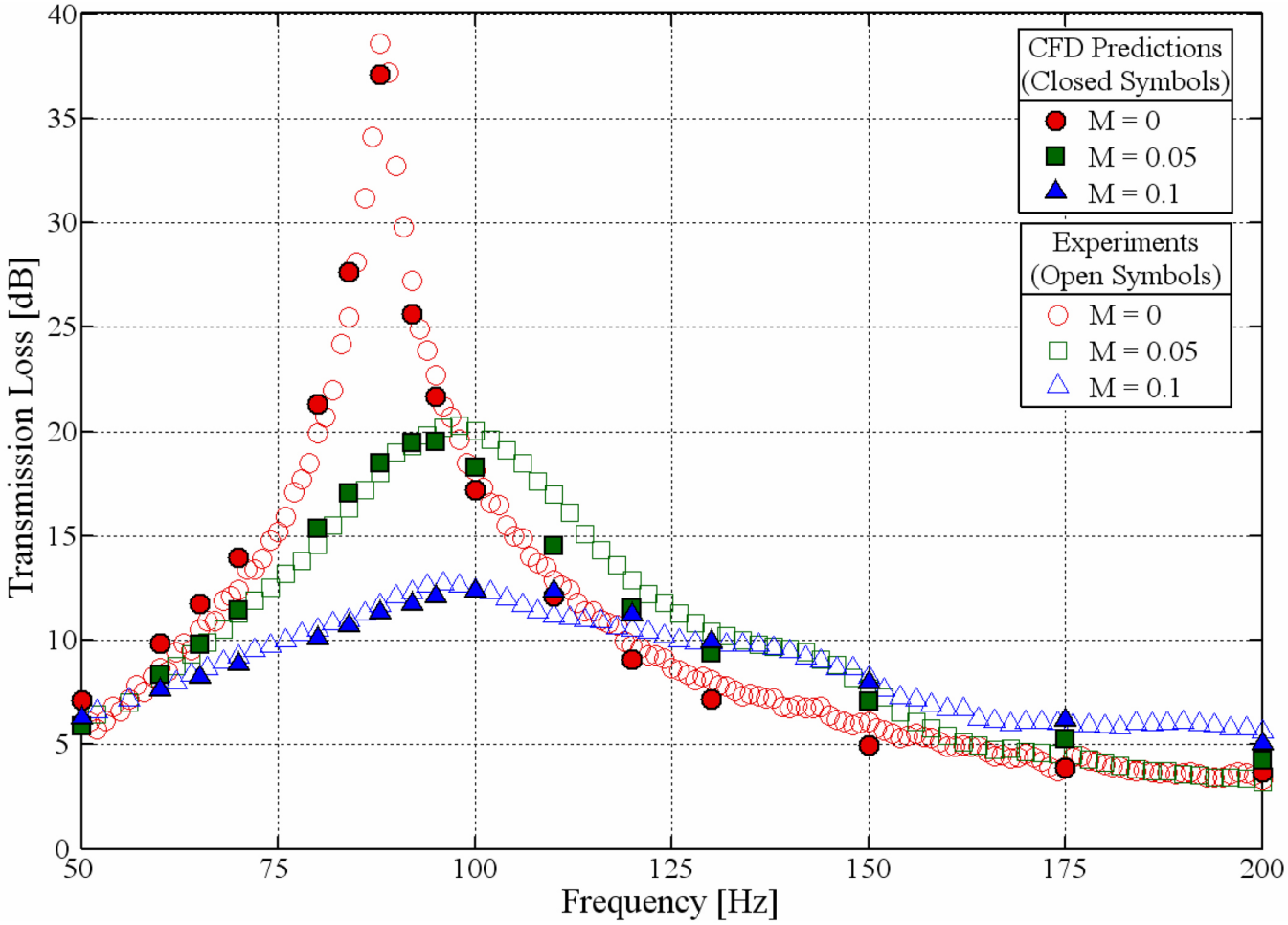

Figure 4. Computational predictions and experimental measurements for transmission loss.

(M = 0.05 and 0.1). Superimposed on the same figure are the experimental results for the same three cases obtained from the unique experimental setup described in the preceding section. Given particularly the complexity of the unsteady flow field, the level of agreement between the predictions and measurements is excellent, with the exception of some deviations slightly above 100 Hz. The dramatic impact of flow on the acoustic attenuation of Helmholtz resonator is clear. The grazing flow over the neck reduces the peak transmission loss significantly while shifting the peak resonance location from its original (no-flow) frequency of 88 Hz to higher values. The ability of 3D CFD predictions to capture these trends closely is particularly promising in light of a large variety of applications involving flow, which would benefit from the computational approach presented here. An alternative visualization for the effect of grazing flow on the transmission loss of the same Helmholtz resonator is presented in Fig. 5.

For illustrative purposes, the pressure variation corresponding to "four microphone locations" is plotted in Fig. 6 as a function of time for the resonance frequency f_r = 88 Hz at three chosen M's. The level of suppression of pressure oscillations is clear in Fig. 6(a) in the process of moving from upstream (locations 1 and 2) to downstream (locations 3 and 4) of the resonator. Examining Figs. 6(b) and 6(c) also reveals increasing downstream pressures with flow. Time variations of pressure on either side of the resonance frequency have been deferred to Appendix A, where the computational domain is driven by oscillations at 60 (Fig. A1) and 120 Hz (Fig. A2). Consistent with transmission loss observations at these two frequencies the pressures are not significantly affected by flow. The spatial distribution of sound pressure level (SPL) throughout the main duct at the resonance frequency f_r = 88 Hz is depicted in Fig. 7 for three M's. Note that the locations of microphones and the resonator neck in the experimental setup are also superimposed on this figure. While the upstream distribution remains fairly unchanged with flow, the downstream SPL increases markedly with the flow, pointing to the fact that flow hinders the ability of this silencer to attenuate sound.

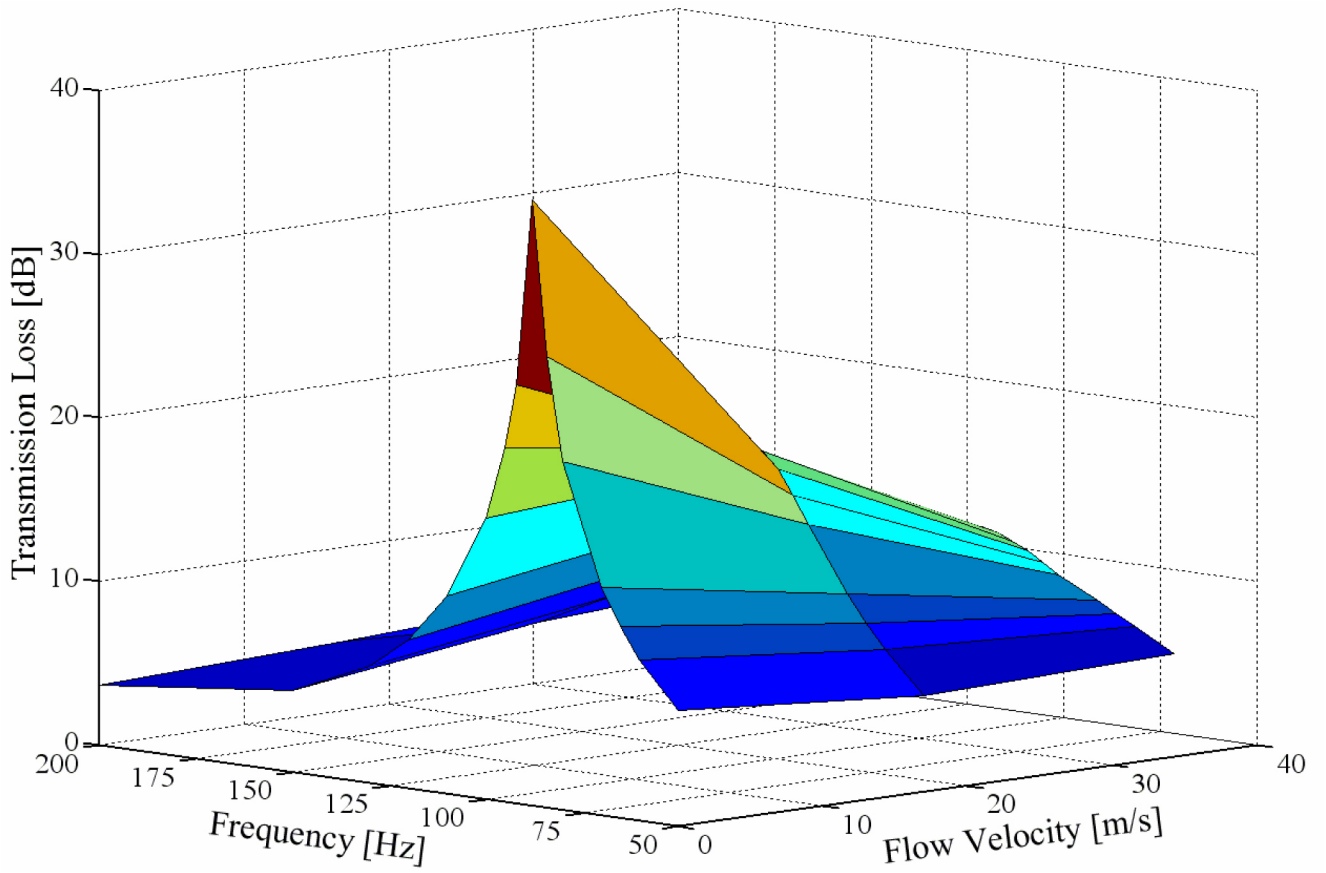

Figure 5. Predicted effect of grazing flow on transmission loss.

To gain further insight into the drastic effect of grazing flow on the attenuation characteristics of the Helmholtz resonator, transmission loss was computed for 10 discrete velocities at the resonance frequency f_r = 88 Hz, as illustrated in Fig. 8. The trend of decreasing transmission loss with mean flow is clear. The predicted sound pressure levels at the "four microphone locations" are also compared in Fig. 9 at the same discrete flow velocities. While the SPL at the upstream locations (1 and 2) remains nearly constant, the SPL at the downstream locations (3 and 4) continues to increase with mean flow, demonstrating the diminishing ability of the Helmholtz resonator to attenuate sound at higher flow velocities.

To investigate the continuous decrease in transmission loss with increasing flow, the acoustic resistance (R'_{ac}) and reactance (X'_{ac}) of the Helmholtz resonator were also computed at the same discrete flow velocities, as illustrated in Figs. 10 and 11, respectively. At f_r = 88 Hz the absolute magnitudes of both R'_{ac} (Fig. 10) and X'_{ac} (Fig. 11) increase with mean flow. As indicated earlier in the Introduction, Phillips [5] and Hersh *et al.* [7] also observed an increase in acoustic resistance with mean flow in their experimental studies. This increase in the acoustic resistance of the Helmholtz resonator explains the decrease in transmission loss, as TL is inversely proportional to the absolute value of $R'_{ac} + iX'_{ac}$.

To examine the details of the influence of flow on the interaction between the Helmholtz cavity and the main duct, animations [22,23] of time-varying velocity were generated computationally for M = 0 and 0.05. In the absence of flow (Fig. 12/Animation 1 [22]) the fluid in the neck influences the flow field beyond the neck, indicating that the effective length of the neck becomes greater than its geometric length, consistent with the well-known "end correction" dating back to Rayleigh [24]. However, introduction of mean flow weakens the communication between the Helmholtz cavity and the main duct as is evident from its domination over the acoustic oscillations in Fig. 13/Animation 2 [23]. The weakening of the cavity-main duct interaction due to mean flow explains the diminishing attenuation of the Helmholtz resonator observed as the reduction in peak transmission loss with increasing flow.

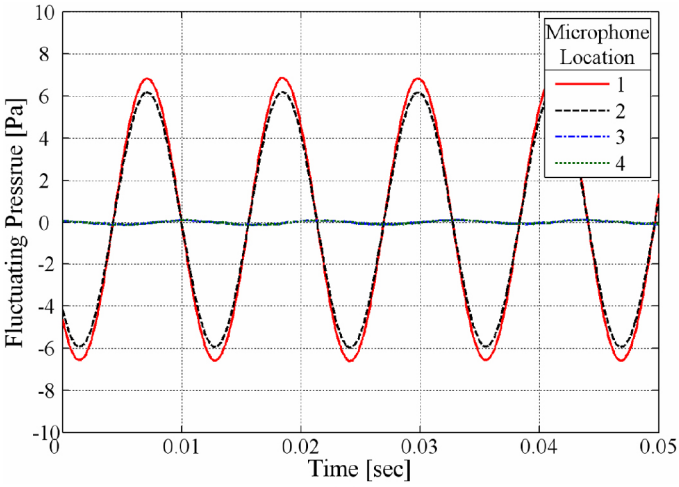

(a)

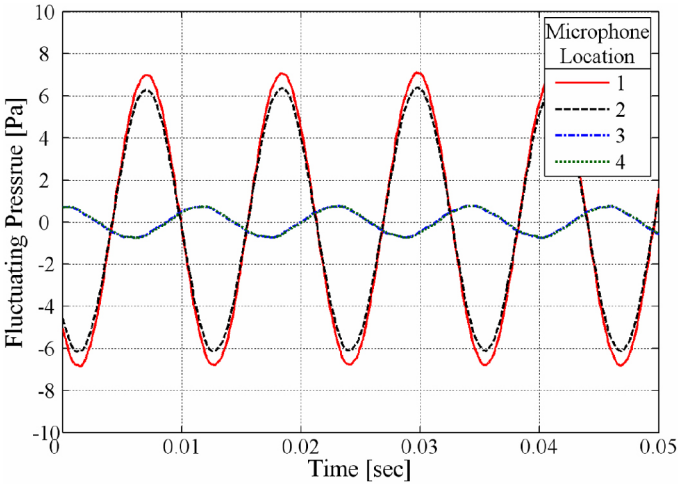

(b)

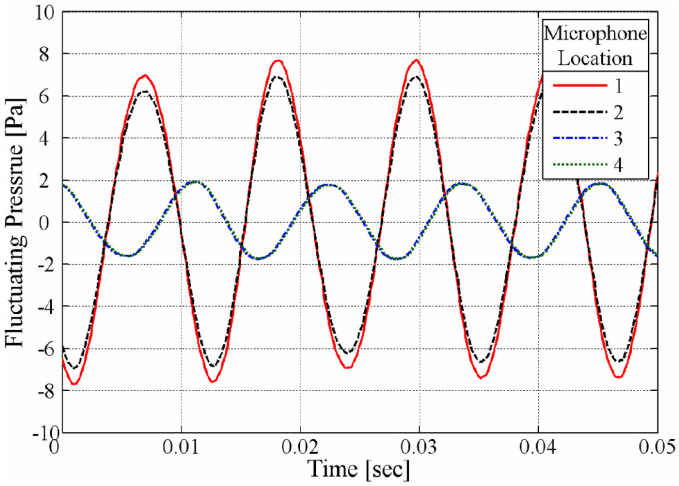

(c)

Figure 6. Predicted pressure fluctuations at locations 1-4 for three flow velocities at f_r = 88 Hz: (a) M = 0, (b) M = 0.05, and (c) M = 0.1.

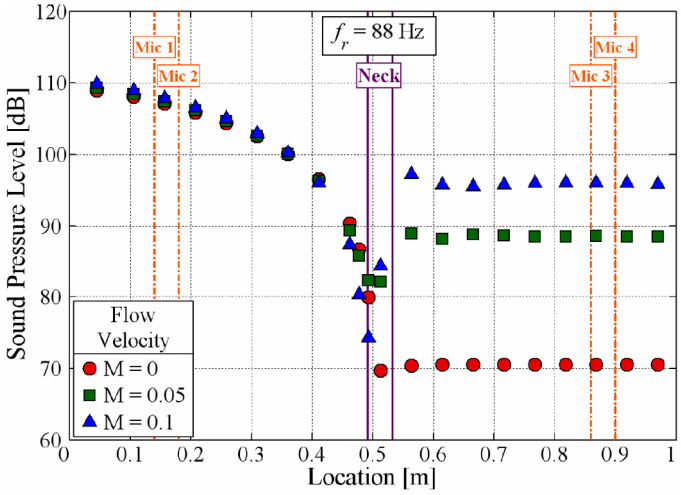

Figure 7. Predicted spatial distribution of sound pressure level in the main duct along x at f_r = 88 Hz.

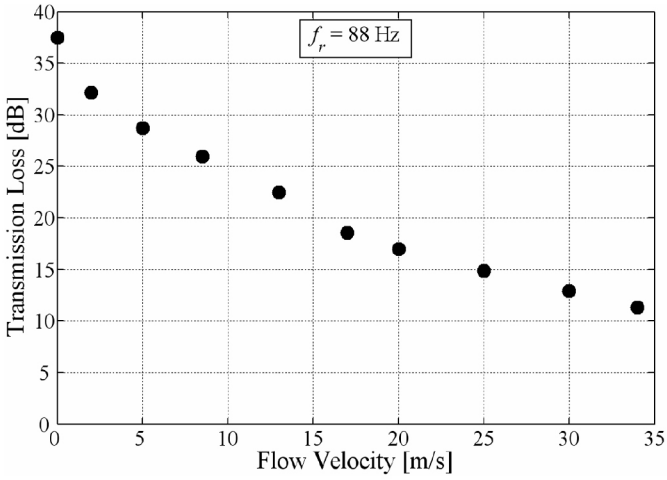

Figure 8. Transmission loss predictions for varying mean flow at f_r = 88 Hz.

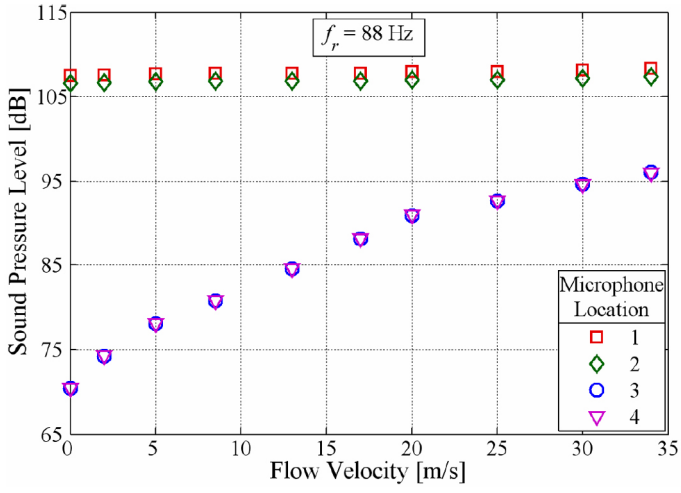

Figure 9. Variation of predicted sound pressure level at locations 1-4 with mean flow at f_r = 88 Hz.

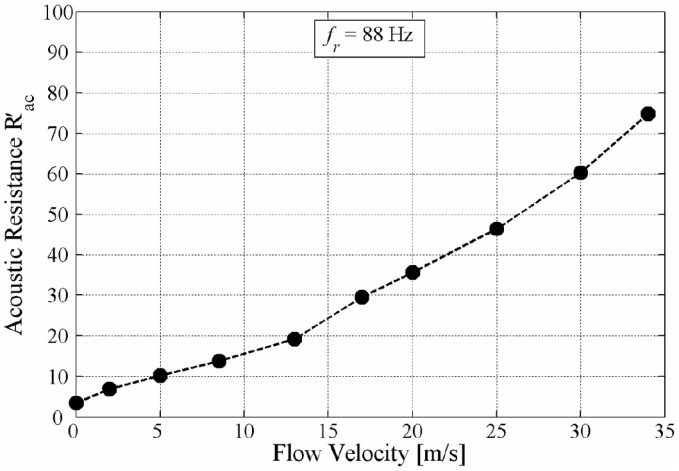

Figure 10. Predicted non-dimensional acoustic resistance varying with flow at f_r = 88 Hz.

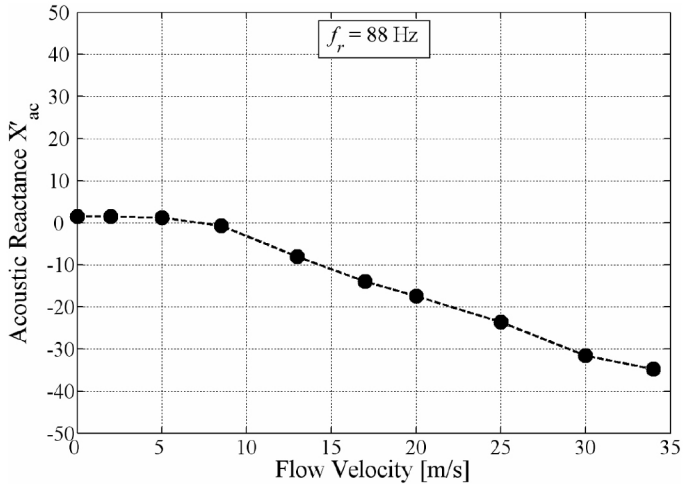

Figure 11. Predicted non-dimensional acoustic reactance varying with flow at f_r = 88 Hz.

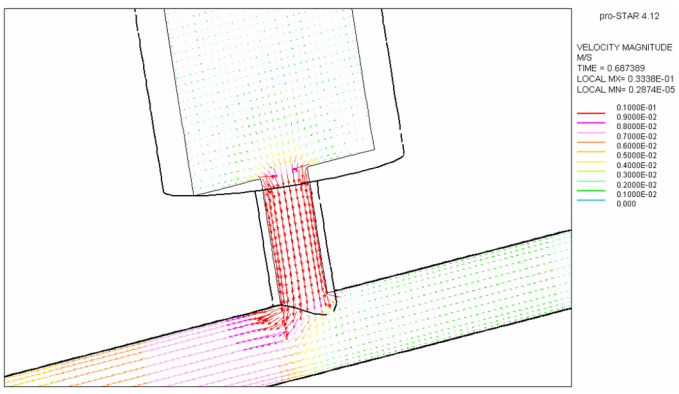

Figure 12. Velocity vectors for M = 0.

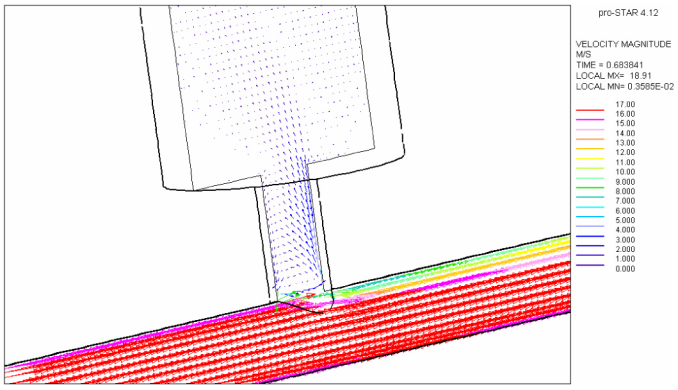

Figure 13. Velocity vectors for M = 0.05.

5. CONCLUDING REMARKS

Three-dimensional CFD has been successfully applied to the prediction of Transmission Loss in Helmholtz resonators subject to grazing flow. These predictions have also been validated in a new flow-impedance tube experimental facility capable of measuring transmission loss in the presence of flow. The level of agreement between the 3D CFD predictions and the experiments for transmission loss demonstrates the effectiveness of the computational approach in determining the complex impact of flow on the acoustics of various components. Available 1D engine simulation codes are usually limited in their ability to capture the effect of flow on the acoustic characteristics of breathing system components. The computational approach adopted here may help overcome some of these limitations, particularly when 1D and 3D CFD codes are coupled. The key observations from the present study are as follows:

- The absolute magnitudes of both acoustic resistance and reactance of the Helmholtz resonator increase with flow, leading to a decrease in transmission loss, as TL is inversely proportional to the absolute magnitude of $R'_{ac} + iX'_{ac}$.
- While the predicted SPL at locations upstream of the Helmholtz resonator remains nearly constant, the continuous rise in SPL at downstream locations with increasing flow, demonstrates the diminished ability of the Helmholtz resonator to attenuate sound at higher flow velocities.
- For the Helmholtz resonator considered here, the introduction of mean flow dramatically weakens the interaction between the cavity and the main duct, resulting in the reduction of peak transmission loss along with the shift in resonance frequency to higher values.

REFERENCES

1. Selamet, A. and Lee, I. J., "Helmholtz resonator with extended neck," Journal of the Acoustical Society of America 113(4):1975-1985, 2003.

2. Selamet, A., Xu, M. B., Lee, I. J., and Huff, N. T., "Helmholtz resonator lined with absorbing material," Journal of the Acoustical Society of America 117(2):725-733, 2005.

3. McAuliffe, C. E., "The influence of high speed air flow on the behavior of acoustical elements," M. S. Thesis, Massachusetts Institute of Technology, 1950.

4. Meyer, E., Mechel, F., and Kurtze, G., "Experiments on the influence of flow on sound attenuation in absorbing ducts," Journal of the Acoustical Society of America 30(3): 165-174, 1958.

5. Phillips, B., "Effects of high-wave amplitude and mean flow on a Helmholtz resonator," NASA Technical Memorandum NASA TM X-1582, 1968.

6. Anderson, J. S., "The effect of an air flow on a single side branch Helmholtz resonator in a circular duct," Journal of Sound and Vibration, 52(3):423-431, 1977.

7. Hersh, S., Walker, B., and Bucka, M., "Effect of grazing flow on the acoustic impedance of Helmholtz resonators consisting of single and clustered orifices," AIAA 11th Fluid and Plasma Dynamics Conference, Seattle, WA, AIAA Paper 78-1124, 1978.

8. Cummings, A., "The response of a resonator under a turbulent boundary layer to a high amplitude non-harmonic sound field," Journal of Sound and Vibration 115(2):321-328, 1987.

9. Ricot, D., Maillard, V., and Bailly, C., "Numerical simulation of the unsteady flow past a cavity and application to the sun-roof buffeting," AIAA Paper 2001-2112, 2001.

10. Tam, C. K. W. and Kurbatskii, K. A., "Microfluid dynamics and acoustics of resonant liners," AIAA Journal 38(9):1331-1339, 2000.

11. Tam, C. K. W., Kurbatskii, K. A., Ahuja, K. K., and Gaeta, R. J.Jr., "A numerical and experimental investigation of the dissipation mechanisms of resonant acoustic liners," Journal of Sound and Vibration 245(3):545-557, 2001.

12. Iqbal, A. and Selamet, A., "A two-dimensional computational study of the flow effect on the acoustic behaviour of Helmholtz resonators," International Journal of Vehicle Noise and Vibration 6(2/3/4): 130-148, 2010.

13. Methodology, STAR-CD (Version 4.12), Computer Software, CD-adapco, Melville, NY, 2009.

14. El Tahry, S. H., "k-ε equation for compressible reciprocating engine flows," AIAA Journal of Energy 7(4): 345-353, 1983.

15. Lien, F. S., Chen, W. L., and Leschziner, M. A., "Low-Reynolds-number-eddy-viscosity modeling based on non-linear stress-strain/vorticity relations," Proceedings of the 3rd Symposium on Engineering Turbulence Modeling and Measurements, Crete, Greece, 1996.

16. Issa, R. I., "Solution of the implicitly discretized fluid flow equations by operator-splitting," Journal of Computational Physics, 62(1):40-65, 1986.

17. Issa, R. I., Gosman, A. D., and Watkins, A. P., "The computation of compressible and incompressible recirculating flows by noniterative implicit scheme," Journal of Computational Physics 62(1):66-82, 1986.

18. Issa, R. I., Ahmadi Befrui, B., Beshay, K., and Gosman, A. D., "Solution of the implicitly discretised reacting flow equations by operator-splitting," Journal of Computational Physics 93:388-410, 1991.

19. Chung, J. Y. and Blaser, D. A., "Transfer function method of measuring in-duct acoustic properties. I. Theory," Journal of the Acoustical Society of America 68(3):907-913, 1980.

20. Chung, J. Y. and Blaser, D. A., "Transfer function method of measuring in-duct acoustic properties. II. Experiment," Journal of the Acoustical Society of America 68(3):914-921, 1980.

21. ASTM E 1050 - 08, "Standard test method for impedance and absorption of acoustical materials using a tube, two microphones and a digital frequency analysis system," American Society for Testing and Material, 2008.

22. Prof. A. Selamet's website for publications, course materials, and research labs, "Animation 1," http://engine.osu.edu/animations/2011/Animationl_M_0_0.gif, December 2010.

23. Prof. A. Selamet's website for publications, course materials, and research labs, "Animation 2," http://engine.osu.edu/animations/2011/Animation2_M_0_05.gif, December 2010.

24. Rayleigh, J. W. S., "The Theory of Sound, Volume II," Dover, New York, 1945.

CONTACT INFORMATION

Corresponding Author:

Prof. Ahmet Selamet
Department of Mechanical Engineering
The Ohio State University
E 509 Peter L. and Clara M. Scott Laboratory
201 West 19th Avenue
Columbus, OH 43210-1142 USA
selamet.1@osu.edu
Ph: 1-614-292-4143
Fax: 1-614-688-4111

DEFINITIONS/ABBREVIATIONS

a_{in}
Amplitude of acoustic velocity at inlet

$\bar{c}_p$
Mean constant pressure specific heat at temperature T

c_p^o
Reference specific heat at temperature T_o

$C_{\varepsilon 1}$, $C_{\varepsilon 2}$, $C_{\varepsilon 4}$
Constants for turbulence equations

C_μ
Empirical coefficient

f
Frequency

f_r
Resonance frequency

h_t
Thermal enthalpy

k
Turbulent kinetic energy

κ
von Karman constant

k
Wavenumber

k_r
Wavenumber for reflected wave component

L_{in}, L_{out}
Inlet/Outlet duct length

M
Mach number

p
Total pressure

P_1, P_2, P_3, P_4
Pressure calculated at microphone locations 1, 2, 3, and 4

$P_1(f)$, $P_2(f)$,
Fourier-transformed acoustic

$P_3(f)$, $P_4(f)$
pressures in frequency domain

$P_d(f)$
Transmitted wave on the downstream side in frequency domain

$P_u(f)$
Incident wave on the upstream side in frequency domain

R
Ideal gas constant

R'_{ac}
Acoustic resistance

s
Microphone spacing

t
Time

T
Temperature

T_o
Reference temperature

u
Velocity in x-direction

u_{in}
Mean flow velocity at inlet

v
Velocity in y-direction

w
Velocity in z-direction

X'ac
Acoustic reactance

y
Normal distance to the nearest wall

GREEK SYMBOLS

δ_{ij}
Kronecker delta

ε
Turbulent dissipation

κ
Thermal conductivity

ν
Kinematic viscosity

ρ
Density

σ_{ε}
Turbulent Prandtl number for ε equation

σ_{k}
Turbulent Prandtl number for k equation

μ
Viscosity

μ_{t}
Turbulent viscosity

ω
Angular frequency, $2\pi f$

ABBREVIATIONS

1D
One-dimensional

2D
Two-dimensional

3D
Three-dimensional

CFD
Computational Fluid Dynamics

DES
Detached Eddy Simulation

DNS
Direct Numerical Simulation

FFT
Fast Fourier Transform

LES
Large Eddy Simulation

PISO
Pressure-Implicit-Splitting-of- Operators

SPL
Sound Pressure Level

TL
Transmission Loss

APPENDIX A

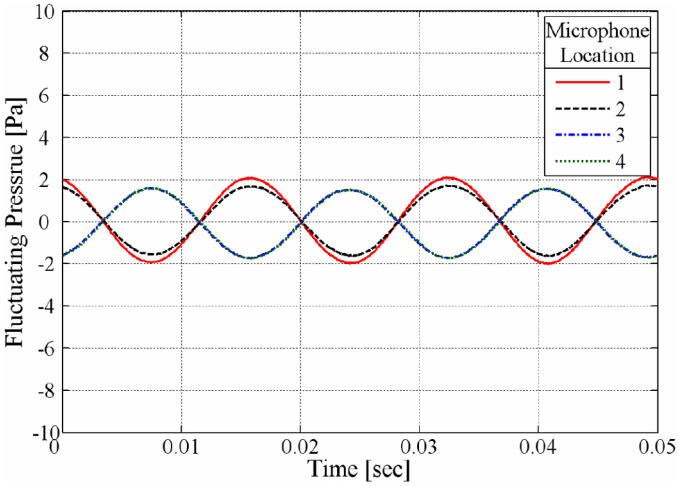

(a)

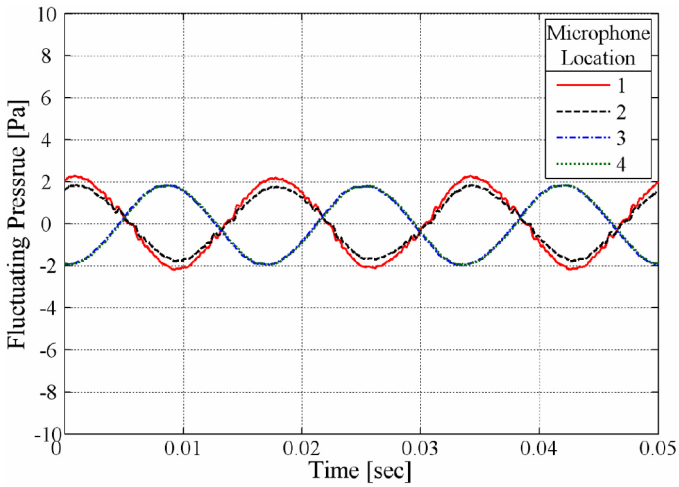

(b)

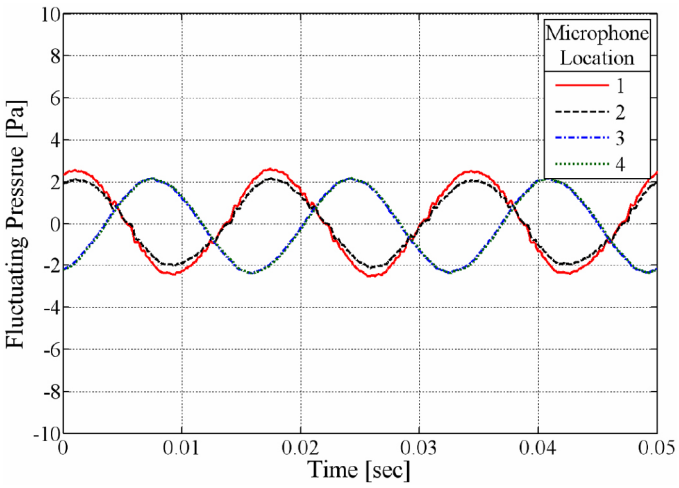

(c)

Figure A1. Pressure fluctuations at locations 1- 4 for three chosen M's at f = 60 Hz: (a) M= 0, (b) M = 0.05, and (c) M = 0.1.

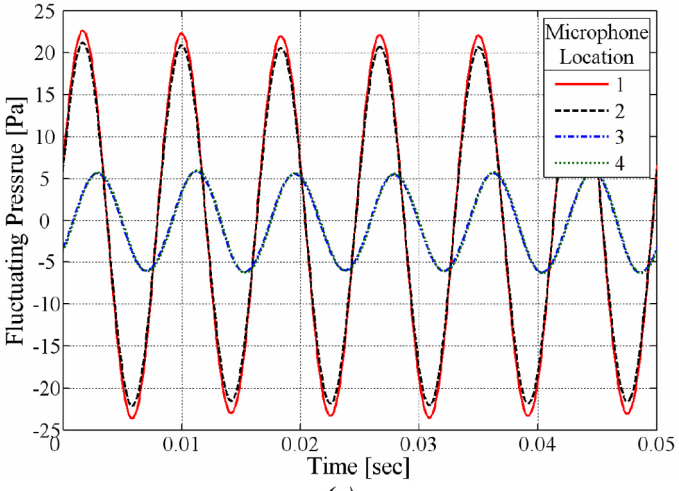

(a)

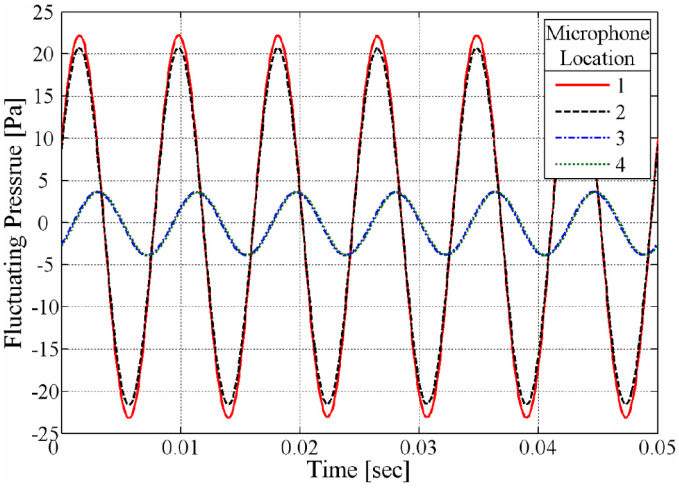

(b)

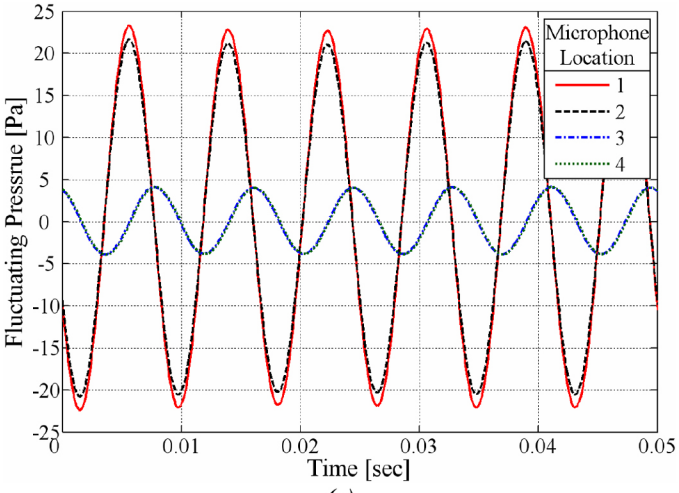

(c)

Figure A2. Pressure fluctuations at locations 1-4 for three chosen M's at f = 120 Hz: (a) M = 0, (b) M = 0.05, and (c) M = 0.1.

ISSN 0148-7191

SAE Customer Service:
Tel: 877-606-7323 (inside USA and Canada)
Tel: 724-776-4970 (outside USA)
Fax: 724-776-0790
Email: CustomerService@sae.org
SAE Web Address: http://www.sae.org
Printed in USA